Ab initio transport across bismuth selenide surface barriers

Awadhesh Narayan,* Ivan Rungger, Andrea Droghetti, and Stefano Sanvito
School of Physics and CRANN, Trinity College, Dublin 2, Ireland
(Received 11 March 2014; revised manuscript received 27 October 2014; published 24 November 2014)

We investigate the effect of potential barriers in the form of step edges on the scattering properties of $Bi_2Se_3(111)$ topological surface states by means of large-scale *ab initio* transport simulations. Our results demonstrate the suppression of perfect backscattering, while all other scattering processes, which do not entail a complete spin and momentum reversal, are allowed. Furthermore, we find that the spin of the surface state develops an out-of-plane component as it traverses the barrier. Our calculations reveal the existence of quasibound states in the vicinity of the surface barriers, which appear in the form of an enhanced density of states in the energy window corresponding to the topological state. For double barriers we demonstrate the formation of quantum well states. To complement our first-principles results we construct a two-dimensional low-energy effective model and illustrate its shortcomings. Our findings are discussed in the context of a number of recent experimental works.

DOI: 10.1103/PhysRevB.90.205431 PACS number(s): 73.63.−b, 73.20.−r, 73.50.Bk, 73.22.−f

I. INTRODUCTION

Bismuth selenide has emerged as the prototypical topological insulator material due to its single Dirac cone in the surface band structure and relatively large bulk band gap. In 2009, concurrent theoretical [1] and experimental [2] works revealed the topological insulator phase of Bi_2Se_3. Since then many fundamental properties of topological states have been demonstrated in this material, which has been called the hydrogen atom of topological insulators [3,4].

In recent years, there has been a rapid expansion in the number of scanning tunneling microscope experiments on the $Bi_2Se_3(111)$ and the closely related $Bi_2Te_3(111)$ surface. Impurities on bismuth selenide have been imaged and scattering mediated by bulk states has been observed [5–8]. Additionally, there have been studies of dopants on the bismuth telluride surface [9,10], and interestingly, a bound state at a surface step of Bi_2Te_3 has also been found [11]. On the theoretical front, there have been several efforts towards modeling the scattering of these surface states from perturbation theory by employing Dirac-like model Hamiltonians and by imposing symmetry considerations [12–14]. Furthermore, a study of the robustness of surface states against on-site disorder by employing first-principles calculations was reported [15]. The problem of scattering at a monolayer-bilayer graphene junction has also been investigated [16].

In this paper, we investigate the effect of step barriers at the $Bi_2Se_3(111)$ surface on the scattering properties of the topological states by means of *ab initio* transport calculations. We find that, due to the spin-polarized helical nature of the surface band, there is no scattering for the normal incidence, since a reflection would entail a 180° backscattering. However, as one moves to a non-normal incidence, scattering is revealed. This is because the spins of the counter-propagating channels are no longer antiparallel. An analysis of the local density of states (LDOS) reveals that the surface barrier strongly affects the spin of the surface state, in particular, allowing an out-of-plane spin component, which is negligible in the absence of the barrier. To allow comparisons with our *ab initio* results we have constructed a potential barrier model based on a simple Dirac Hamiltonian for the surface states. This is solved for barriers of various shapes and a comparison is made with our first-principles calculations. We note in passing that, although our *ab initio* calculations have been performed for the particular case of bismuth selenide, we expect the same qualitative results also to hold for step edges perpendicular to directions without hexagonal warping in Bi_2Te_3 and for other related materials like Bi_2Te_2S and $TlBiSe_2$.

The remainder of the paper is organized as follows. We describe our computational methods in Sec. II; in particular, we outline the procedure for performing the transport calculations. In Sec. III we then study scattering originating from a single surface barrier by analyzing the transmission and the densities of states. Intriguingly, our calculations reveal a bound state in the vicinity of the barrier, and we study its energy dispersion. From there, we move on in Sec. IV to construct a low-energy model for the scattering problem, with the barrier strength and width extracted from our *ab initio* results. Next we look at the analogous problem in the presence of double barriers of different lengths in Sec. V. Notably, we find an energy splitting of the bound state when the states at the two barriers interact directly as in the case of a short double barrier, as well as when the bound states couple with quantum well states formed in the case of a longer double barrier. Finally, we summarize our results and conclude in Sec. VI.

II. COMPUTATIONAL METHODS

Our transport calculations have been performed using the SMEAGOL code, which combines the density functional theory numerical implementation contained in the SIESTA code [17] with the nonequilibrium Green's function method for electron transport. Here we briefly outline the calculation procedure and refer the readers to Refs. [18–20] for a more detailed exposition. In SMEAGOL semi-infinite electrodes are attached to a central scattering region by means of self-energies. The calculation of the self-energies of the leads is performed using a singular-value decomposition-based, robust and efficient algorithm, which overcomes the problems related to recursive methods [20]. The Hamiltonian needed for the algorithm is calculated using an equivalent infinite-bulk system. The

*narayaa@tcd.ie

transport calculation proceeds by using the density matrix and the Kohn-Sham Hamiltonian obtained from SIESTA. The self-energies for the leads are added to the Hamiltonian of the scattering region, H, and the nonequilibrium Green's function is obtained by direct inversion,

$$G(E) = [E + i0^+ - H - \Sigma_{\rm L} - \Sigma_{\rm R}]^{-1}, \quad (1)$$

where Σ_α is the self-energy of the left-hand side ($\alpha = {\rm L}$) and right-hand side ($\alpha = {\rm R}$) leads. The charge density is then calculated by integrating the nonequilibrium Green's function along a contour in the complex energy plane,

$$\rho(E) = \frac{1}{2\pi i}\int dE G^<(E), \quad (2)$$

where $G^<(E) = iG[f_{\rm L}\Gamma_{\rm L} + f_{\rm R}\Gamma_{\rm R}]G^\dagger$ is the lesser Green's function for the transport problem. The Fermi functions for the leads are denoted f_α and $\Gamma_\alpha = (\Sigma_\alpha - \Sigma_\alpha^\dagger)$ are the broadening matrices. In order to perform the contour integral in Eq. (2) we use 16 energy points in the complex semicircle, 16 points along the line parallel to the real axis, and 16 poles. The density matrix calculated in Eq. (2) is used by SIESTA to re-evaluate the Kohn-Sham Hamiltonian, and this procedure is iterated until self-consistency is obtained. Once convergence is achieved, the relevant quantities like the transmission function, $T(E)$, and the density of states (DOS), $\mathcal{N}(E)$, are calculated,

$$T(E) = {\rm Tr}[\Gamma_L G^\dagger \Gamma_R G], \quad \mathcal{N}(E) = \frac{1}{2\pi}{\rm Tr}[A(E)S], \quad (3)$$

where Tr stands for the trace, $A(E) = i(G - G^\dagger)$ is the spectral function, and S is the overlap matrix.

In all calculations spin-orbit interaction is included by means of an on-site approximation [21] and the Perdew-Burke-Ernzerhof generalized gradient approximation (GGA) to the exchange-correlation functional is employed [22]. We have used a double-ζ polarized basis set and a real-space mesh cutoff of 300 Rydbergs. For slab calculations a minimum 25-Å vacuum region has been included to prevent spurious interaction between periodic replicas. We use $3 \times 1 \times 1$ k-point mesh to obtain the self-consistent potential (here x is the direction perpendicular to the transport direction in the plane of the slab, y is along the slab height, and z is the transport direction). When calculating the integrated transmission and DOS we use 101 k points along the x direction. Periodic boundary conditions have been considered in the plane orthogonal to the transport direction, while using open boundary conditions along the transport direction allows us to simulate a single scatterer, which, in this particular case, is a surface step.

The unit cell used for the leads is shown in Fig. 1(a). We note that by adding the self-energies obtained from such quasi-two-dimensional leads to the Hamiltonian of the scattering region, one avoids any finite-size effects. It consists of a slab three quintuple layers (3 QL) thick terminated on both sides by Se atoms, as found experimentally. For the slab we use the experimental lattice constants. The corresponding band structure is shown in Fig. 1(b). Note that there is band folding as a consequence of the doubling of the Bi_2Se_3 primitive unit cell. The band structure reveals the Dirac cone and the helical states consistent with earlier studies [1]. It should also be noted that there is a small but finite gap (of the order of 0.015 eV)

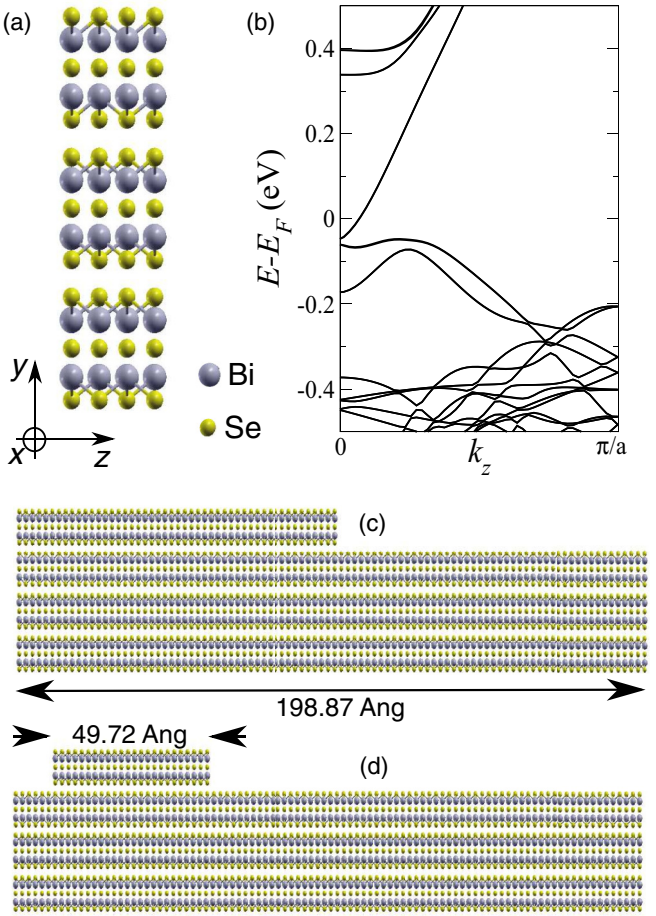

FIG. 1. (Color online) (a) The unit cell of the 3-QL slab leads used in the transport calculations, corresponding to a periodic quasi-two-dimensional system. The smaller (yellow) and larger (purple) spheres represent selenium and bismuth atoms, respectively. The slab is terminated on both sides by Se. (b) The band structure along the transport direction, z, is shown at $k_x = 0$. The surface band in the energy window $[-0.05, 0.30]$ eV has a helical spin texture, with the spin locked in the momentum direction. The transport setup for the scattering problem is shown for (c) a single barrier and (d) a double barrier. In both cases we add an extra single-QL-high barrier on the 3-QL-thick slab. Note that the same self-energies for semi-infinite 3-QL leads are attached on the left and right sides of the scattering region in (d), while different left and right electrodes, corresponding to 4-QL and 3-QL slabs, are needed in (c).

at the Γ point in the cone due to interaction between the two surfaces at opposite sides of the slab. However, this small gap does not affect our analysis of the topological states at higher energies, since the tunneling between the two surfaces is negligible, as we elaborate in the next section. The transport setup for single and double barriers is shown in Figs. 1(c) and 1(d), respectively. We consider a single-QL-high barrier on a 3-QL-thick slab. The step edge is extended along the Γ-M direction and the transport is along the orthogonal Γ-K direction of the primitive Bi_2Se_3 Brillouin zone. The scattering region has a length of 198.87 Å. For the single-barrier case the 4-QL region extends over about half the length of the scattering region. For the double-barrier setup we investigate two barrier lengths, where the step extends over a region of 49.72 Å in

the shorter case and is 149.16 Å for the longer one. Note that such large cells comprising a few thousand atoms require an accurate order-N algorithm such as the one available in SMEAGOL [23].

III. SCATTERING FROM A SINGLE BARRIER

We begin our analysis by looking at the transport across a single surface barrier [see Fig. 1(c)], for which the transmission function is shown in Fig. 2(a) as a function of energy and for different values of the x component of the wave vector. At normal incidence ($k_x = 0$), the surface states are perfectly transmitted, $T = 2$, due to their helicity. As such, our first-principles calculations confirm Klein tunneling [24]. The transmission of bulk states, however, is reduced by the presence of the step edge. In contrast, as soon as one moves away from normal incidence, the transmission is no longer integer-valued. In particular, it dips below $T = 2$, indicating

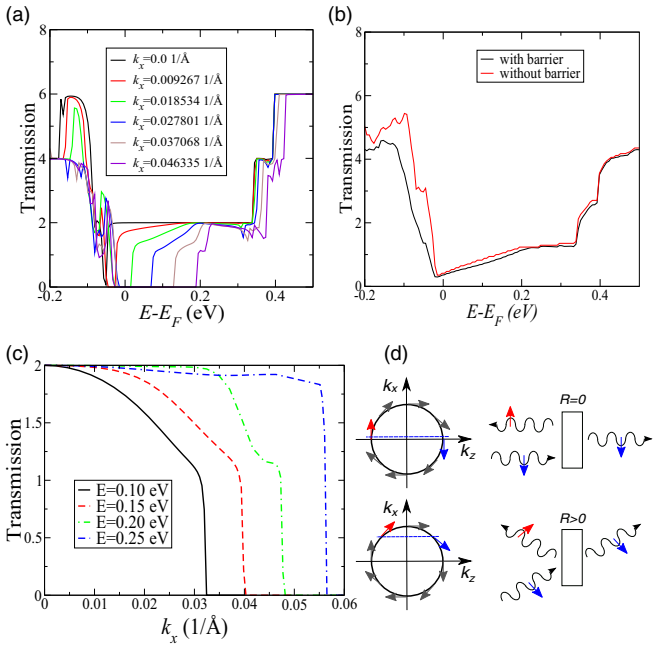

FIG. 2. (Color online) (a) Transmission across the surface barrier as a function of energy at different values of the x component of the wave vector, orthogonal to the transport direction. Different curves correspond to different k_x, starting from $k_x = 0$ up to $k_x = 0.046\,335$ Å^{-1}, in equal steps of $0.009\,267$ Å^{-1}. Note the perfect transmission at $k_x = 0$. At other incidence angles, T is reduced. (b) The total transmission integrated over k_x in the presence (black curve) and absence [gray (red) curve] of the barrier. (c) The transmission as a function of k_x, at different constant energy cuts in the energy region of the surface states. Note that T is reduced from $T = 2$ at a nonzero angle of incidence and, with sufficiently large k_x, drops down towards $T = 1$. Upon further increase in k_x, the band edge for the Dirac cone at the bottom surface is reached, and the transmission abruptly goes to 0. Nonzero reflection at the barrier can be explained using the schematic in (d). At non-normal incidence there is a finite overlap between the spin projections of the forward- and backward-moving surface states. Backscattering at angles away from normal incidence is present even in the absence of time-reversal symmetry-breaking perturbations.

substantial scattering. Note that the drop in transmission at $k_x = 0$ and $E - E_F = -0.05$ eV is merely due to the small gap in the band structure due to the finite thickness of the slab. Figure 2(b) shows the total transmission obtained by integrating $T(E,k_x)$ over all angles of incidence, namely, $T_{\text{total}} = \frac{1}{\Omega_{\text{BZ}}} \int_{k_x} T(E,k_x)dk_x$, where Ω_{BZ} is the length of the Brillouin zone (BZ). Notably T_{total} retains the characteristic "V shape" associated with the linear Dirac cone-like bands, despite the presence of the barrier. Overall we can conclude that the total transmission in the presence of the barrier is quite close to the one for the unperturbed slab [compare the gray (red) and black curves in Fig. 2(c)]. For comparison, we have also performed calculations for steps running along the Γ-K direction (with transport along Γ-M). Since the hexagonal warping effect, particularly at energies close to the Dirac crossing, is quite small in Bi_2Se_3, we find results which are very similar to the ones obtained for steps along the Γ-M direction. Hence, in the rest of this paper we focus our attention on the latter.

At non-normal incidence the spin projections of the surface states counter-propagating at a given edge are no longer antiparallel and thus backscattering becomes allowed, even in the absence of a perturbation that breaks time-reversal symmetry. We note that, although spin-orbit coupling mixes the spin components, one can still define spin components along different directions by using a projection onto the three Pauli matrices $\{\sigma_x,\sigma_y,\sigma_z\}$ and the identity matrix I. The situation is schematically illustrated in Fig. 2(d), and its consequences are demonstrated in Fig. 2(c), where we plot the transmission across the surface barrier as a function of k_x at different energies. Clearly $T(E,k_x)$ is reduced as k_x increases, which is expected from the argument related to the spin projections of the two counter-propagating surface states. At larger incidence angles the transmission tends towards the residual value of 1, since a perfectly transmitted surface state is present at the opposite side of the slab (no scattering center is present on the opposite surface). If one increases k_x even further, the band edge for the Dirac cone at both surfaces is reached, and the transmission abruptly goes to 0. It can be shown that the maximum scattering amplitude is proportional to $\frac{1}{2}(1 + \cos\theta)$, where θ is the angle between the spin directions of the counter-propagating surface states [25]. Note that at higher energies, the transmission persists at values around the unperturbed one, $T = 2$, for larger incidence angles. This is because as one moves the Fermi level at higher energies, the Fermi circle gets larger. Consequently, the same k_x corresponds to a smaller incidence angle.

In scanning tunneling microscope experiments, one measures the oscillations in the electron density in order to study the scattering arising from surface modifications, for example, from surface steps as studied in Ref. [26]. A Fourier transform of the density yields the characteristic frequencies of its oscillations, i.e, gives the scattering wave vectors, $q = |k_{\text{inc}} - k_{\text{ref}}|$ (k_{inc} and k_{ref} are incident and reflected wave vectors, respectively). In Fig. 3 we plot the density of states projected onto the surface atoms along the scattering region. At $k_x = 0$ no oscillations in the projected DOS (PDOS) are seen after reflection from the step edge. However, moving away from normal incidence, the above-mentioned oscillations begin to appear. We remind the reader that along the transport direction (z) the use of self-energies corresponding to the

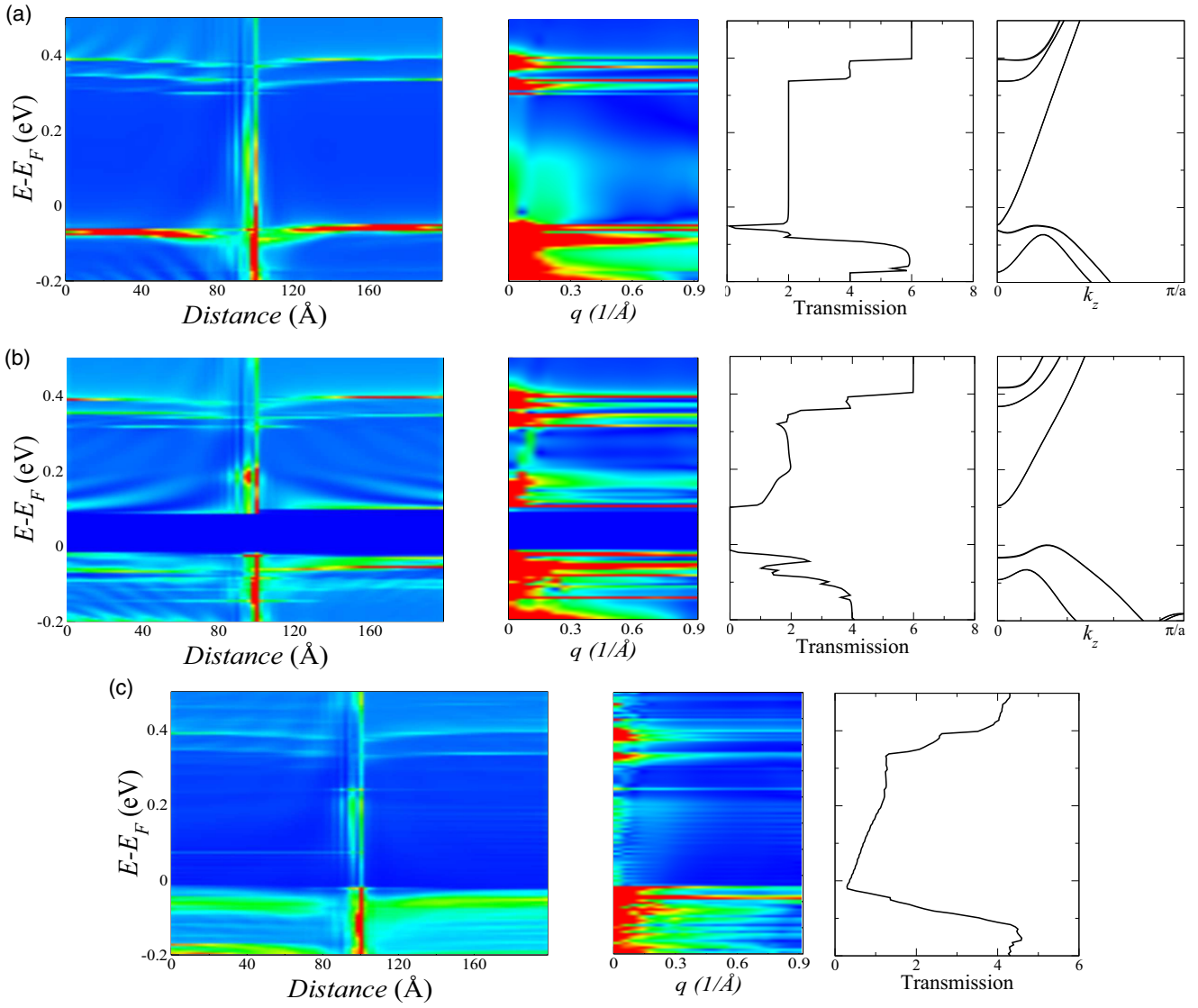

FIG. 3. (Color online) The DOS projected on the surface atoms along the scattering region at (a) $k_x = 0$, (b) at $k_x = 0.032$ Å^{-1}, and (c) integrated over all k_x. At $k_x = 0$ there are no oscillations. These start to emerge at $k_x = 0.032$ Å^{-1} but are not visible in the average. Note in all panels the enhanced DOS on the left-hand side of the barrier. The second column of panels shows the Fourier transform of the projected DOS in the flat region adjacent to the barrier, at the corresponding k_x. The scattering vector resulting from backscattering at non-normal incidence is clearly shown in (b). The average, however, reveals no scattering. Here and henceforth warmer colors represent higher, and cooler colors indicate lower, values. The third column of panels shows the transmission as a function of energy for the three cases. For $k_x = 0$ and $k_x = 0.032$ Å^{-1}, we also plot the band structure along the transport direction for comparison.

left-hand-side and right-hand-side electrodes makes the system infinite but nonperiodic. Thus no finite-size effects, orthogonal to the step direction, on the density oscillations are seen. The scattering vectors can be obtained by performing a Fourier transform of the DOS along the long flat region adjacent to the barrier. At $k_x = 0$, expectedly there are no prominent scattering processes. As one moves to $k_x = 0.032$ Å^{-1}, a dominant scattering wave vector in the Fourier transform appears, starting at 0.1 eV and extending upwards in energy, as shown in Fig. 3(b). This corresponds to backscattering at a non-normal incidence angle. Furthermore, this can be mapped to the band structure along the transport direction, where a band starting at the same energy is present. The average over k_x, however, reveals no scattering on this scale, even though there is a clear backscattering at individual k_x. In order to accurately resolve the small density oscillations above the average, one would need to consider many more k_x points in the calculation. This is computationally prohibitively expensive for the system sizes considered here, and a more detailed investigation of the oscillations will be reported elsewhere [27]. For all three cases we also plot the transmission as a function of energy, for comparison with the surface PDOS.

Figure 3 also makes apparent the band bending (of the order of 0.04 eV) introduced by the step. We show in the next section that such band bending close to the step is a crucial ingredient for constructing a scattering model. Far enough from the step, however, the PDOS reverts to the unperturbed value within ∼40 Å, consistent with experimental observation [28].

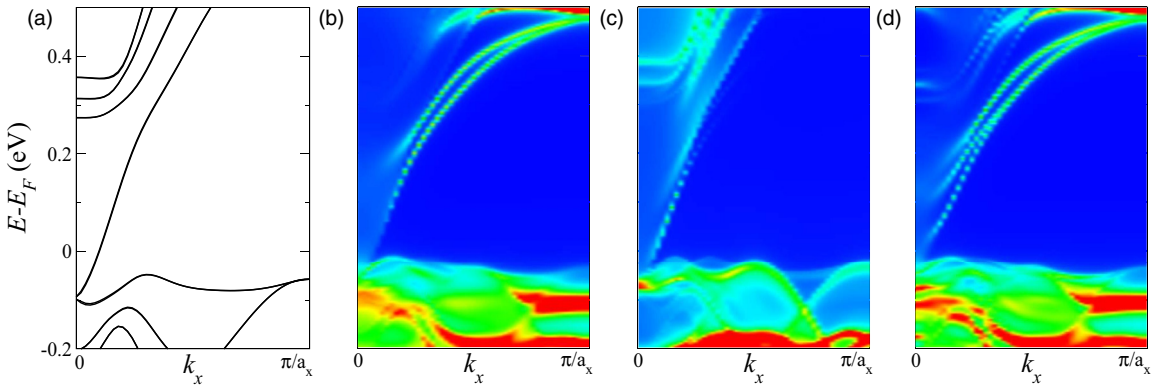

FIG. 4. (Color online) (a) Energy dispersion along k_x (perpendicular to the transport direction) for a perfect periodic system comprising a 4-QL slab, (b) energy dispersion at the single barrier, and (c) energy dispersion 50 Å away from the single barrier. In (b)–(d) color plots show the projected density of states (PDOS) on the atom present at the barrier and an atom 50 Å away from the barrier and the PDOS on the atom at the double barrier (see Sec. V for a discussion). In (b) and (d) note the additional pair of interface states outside the Dirac cone, which merge with it around 0.2 eV.

In contrast to similar steps on the Sb(111) surface [29,30], in Bi_2Se_3 we find bound states close to the step edge and penetrating into the barrier (with an exponentially damped oscillating amplitude). These exist over the entire energy window in which the surface states are present. Similar features with an enhanced DOS have been measured by Alpichshev *et al.* [11] around the surface barrier at the Bi_2Te_3 surface. Importantly, such a bound state was not ascribed to the warped band structure of Bi_2Te_3. Our results point towards a similar bound state in Bi_2Se_3 as well. In the experiment, no information could be obtained about the DOS on the lower side of the step. Our calculations in fact reveal that the state exists only on the higher side of the barrier, and the lower side has no such features. We have also calculated the energy dispersion of this state along the direction perpendicular to the transport. We plot the energy and k_x dependence of the PDOS on the Se atom at the barrier [shown in Fig. 4(b)] and on a surface atom 50 Å away from the barrier [Fig. 4(c)] and compare them to the band structure for the perfect periodic system [Fig. 4(a)]. For the atom present at the barrier we find an additional pair of states outside the unperturbed Dirac bands, which is consistent with topological band theory. These additional states merge into the Dirac cone at $E - E_F \approx 0.2$ eV and produce an enhanced PDOS around that energy. Away from the barrier, however, the PDOS is very similar to that of the unperturbed system, consistent with the pair of bound states being present only close to the barrier. We believe that these predictions of the bound state in Bi_2Se_3 and its energy dispersion may find verification in future experiments.

By analyzing the PDOS of the atoms at the bottom surface we have checked that significant scattering occurs only at the top one; i.e., it is caused by the presence of the step edge, and not due to the tunneling back to the bottom surface. In Fig. 5 we plot the PDOS on the atoms present at the bottom surface at normal incidence and at a representative value of $k_x = 0.032$ Å^{-1} for oblique incidence. For both cases we can see the absence of density oscillations in the energy range corresponding to the surface bands. Notably, no signature of the bound state is observed either. Furthermore, we evaluate the Fourier transform of the PDOS in the flat region next to the step and find no features which may be mapped back to the scattering wave vector q, in contrast to the case of the top surface.

The LDOS associated with electronic states incoming from the left-hand-side lead at 0.175 eV above the Fermi level are shown in Fig. 6 [31]. These clearly illustrate the three-dimensional nature of the path that electrons must traverse

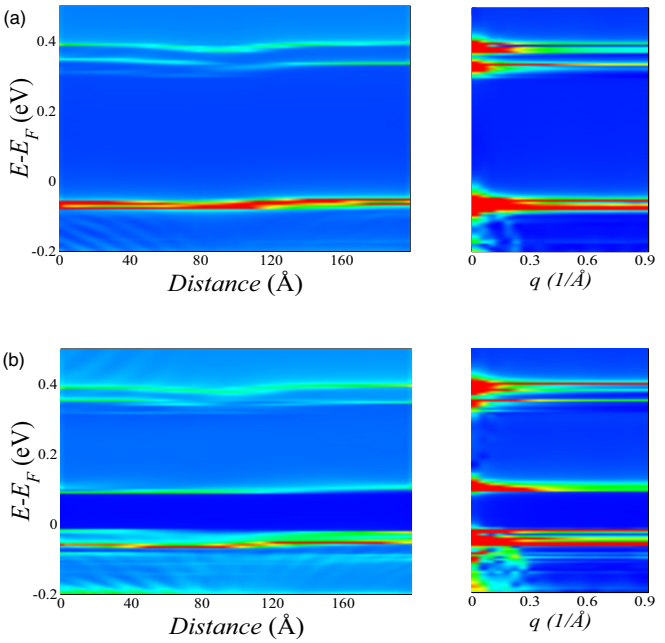

FIG. 5. (Color online) The DOS projected on the bottom surface atoms along the scattering region at (a) normal incidence $k_x = 0$ and (b) an oblique incidence $k_x = 0.032$ Å^{-1}. Note the absence of density oscillations in the bulk energy gap window, even at non-normal incidence. Panels on the right show the Fourier transform of the projected DOS in the flat region adjacent to the barrier. A comparison with Fig. 3 shows the absence of both bound states as well as the signature of dominant scattering vectors in the aforementioned energy range. This illustrates a small coupling between the two surfaces of the Bi_2Se_3 slab investigated in this work.

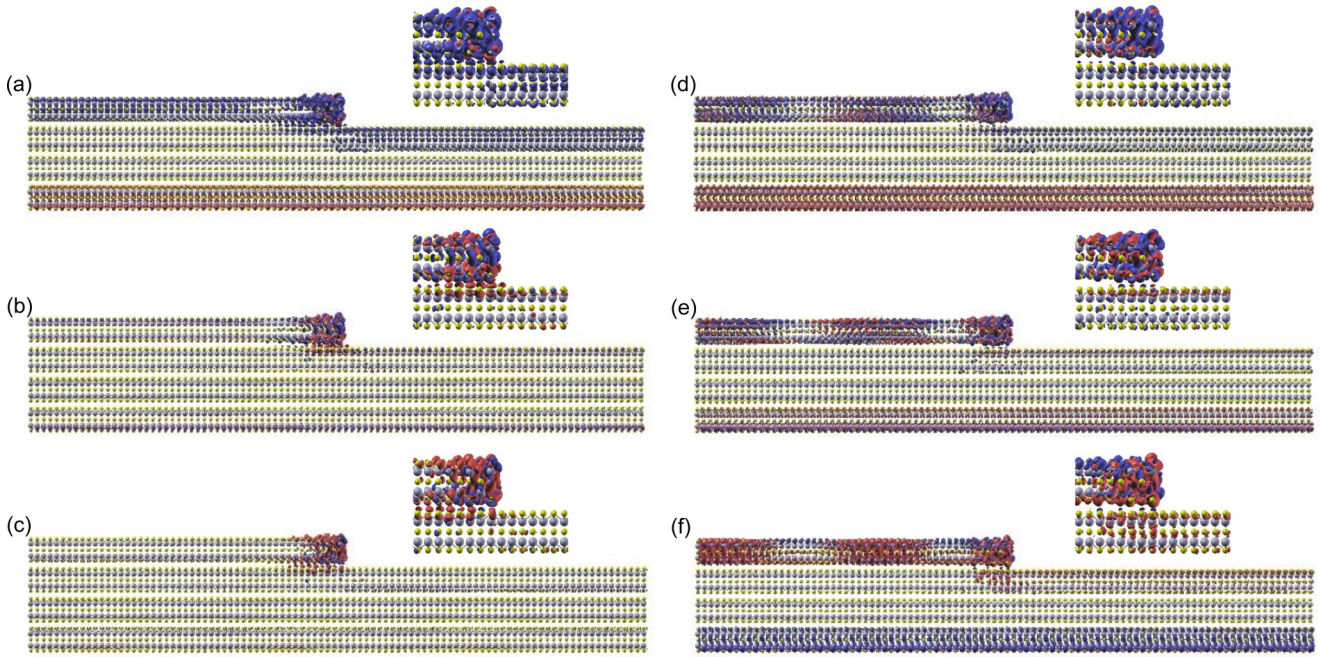

FIG. 6. (Color online) The spin-resolved local density of states (LDOS) for states incoming from the left-hand lead with an energy 0.175 eV above the Fermi level. We plot the spin projection along the (a) x, (b) y, and (c) z directions at $k_x = 0$. (d), (e), and (f) are the corresponding plots for $k_x = 0.032$ Å^{-1}. Here red represents positive values, while blue stands for negative ones. Scattering at the step edge even at $k_x = 0$ allows the spin to rotate out of the plane of the slab, resulting in finite y and z components, in contrast to the unperturbed bottom surface, where these are negligible. At non-normal incidence ($k_x = 0.032$ Å^{-1}) the z component of the spin-resolved LDOS becomes finite, while the step edge introduces a nonzero y component. Insets: Zooms around the step edge.

while crossing the barrier. The spin projections of the LDOS at $k_x = 0$ and $k_x = 0.032$ Å^{-1} are shown in the left and right panels, respectively. In contrast to pristine bismuth selenide, the spins of the helical surface states are no longer confined to the plane of the slab. In the vicinity of the barrier they rotate out of the plane (the y component becomes finite). The LDOS at the bottom unperturbed surface provides a convenient comparison to the pristine surface, albeit with the spin directions reversed. At $k_x = 0.032$ Å^{-1}, the x and z components are dominant for the bottom surface, while the step edge introduces a component along the y direction comparable with the other two, at the top surface. A zoom close to the step shows a large DOS close to the step edge, which is due to the bound state.

IV. A LOW-ENERGY MODEL

In order to interpret our *ab initio* results we construct a simple potential barrier model for the scattering problem. The surface states are described by a Dirac Hamiltonian [1],

$$\mathcal{H} = \epsilon_0 \mathbb{I}_{2\times 2} + \begin{pmatrix} V(z) & v(k_z - ik_x) \\ v(k_z + ik_x) & V(z) \end{pmatrix}, \qquad (4)$$

where the potential profile $V(z)$ is shown in Fig. 7(a). The values of $\epsilon_0 = -0.05$ eV and $v = 4.58$ eVÅ, are obtained from our first-principles band structure. Here we consider only the upper part of the cone; i.e., $E = V(z) + \sqrt{k_z^2 + k_x^2}$. The corresponding eigenstate is given by

$$\psi(k_x, k_z) = \frac{1}{\sqrt{2}} \begin{pmatrix} 1 \\ \frac{k_z + ik_x}{\sqrt{k_z^2 + k_x^2}} \end{pmatrix} e^{i\mathbf{k}\cdot\mathbf{r}}. \qquad (5)$$

One can then use the wave-function continuity conditions at the potential steps to solve for the transmission and reflection coefficients in a straightforward manner. The potentials in the 4-QL and 3-QL leads, V_1 and V_4, respectively, are nearly identical and are set to 0. V_2 is the potential associated

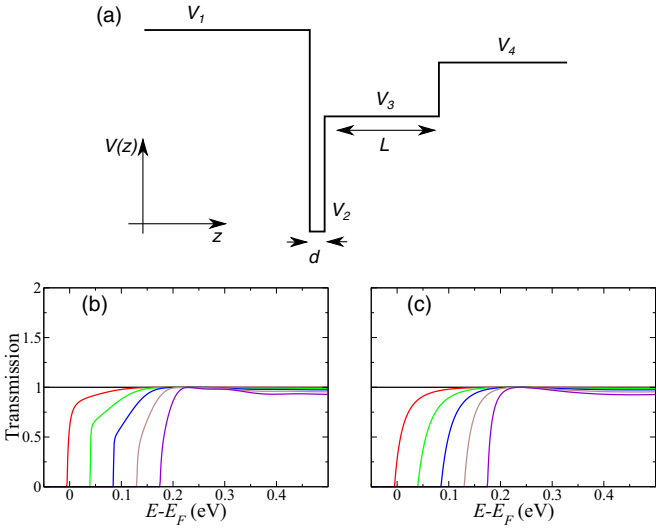

FIG. 7. (Color online) (a) Potential profile for the Dirac model. The parameters are fitted to the *ab initio* results as follows: $V_1 = V_4 = 0$, $V_2 = -1.17$ eV, $d = 20$ Å, and $L = 60$ Å. The transmission as a function of energy is shown for (b) $V_3 = -0.02$ eV and (c) $V_3 = 0.0$ eV. Different curves correspond to different k_x points, with the same definition as used in Fig. 2(a).

with the barrier and extends over a length d, while V_3 is the band bending, which is finite over a distance L. The calculated transmission curves are plotted in Fig. 7(b) for $V_3 = -0.02$ eV and in Fig. 7(c) for $V_3 = 0$. The shape of the transmission function is much closer to that obtained from the *ab initio* calculations for finite $V_3 = -0.02$ (this value of V_3 is chosen from our first-principles results), compared to the situation where $V_3 = 0$. While this comparison does not provide definite evidence of the importance of band bending, it serves as an illustration that it is one of the factors which need to be considered when performing a quantitative modeling of step edges on topological insulator surfaces. Although it appears that this simplified model can qualitatively reproduce the transmission obtained from first principles, a more careful analysis shows that it neglects a number of important aspects of the scattering problem. It does not take into account the three-dimensional nature of the barrier, and as a consequence, it cannot capture the change in spin orientation of the surface states near the barrier. Moreover, it needs as an input the values of the scattering potentials, which an atomistic description is capable of providing, while also capturing the fine details of the scattering process. We also note that several models have been proposed to study topological states on a curved surface. These predict no backscattering at any angle from hyperbolic steps [32,33]. Unfortunately, these models are not valid for the atomic-scale abrupt steps that we have studied in this work.

V. SCATTERING FROM DOUBLE BARRIERS

We now analyze the scattering properties of double-barrier structures constructed over the $Bi_2Se_3(111)$ surface. The scattering region is shown in Fig. 1(d) for the shorter surface barrier. This time the scattering structure is connected on both sides to two identical semi-infinite leads (3-QL slabs). As before, we begin by looking at the transmission across the surface as shown in Fig. 8(a). Again, counter-propagating spin-momentum-locked states yield a perfect transmission at normal incidence. As discussed for the single-barrier case, at finite k_x the transmission is then reduced. However, in contrast to the previous analysis, there are also resonant energies at which the transmission reaches the value of 2; i.e., there is no reflection. At these particular energies the system displays Fabry-Perot resonances, which are characteristic of one-dimensional scattering from double-potential barriers. In Fig. 8(b) we plot the transmission as a function of the incident k_x for different energies. Away from the resonances the transmission again shows a cosine-like behavior, with transmission going down to $T = 1$ as the incidence angle increases (k_x gets larger). At even larger k_x (not shown) the transmission drops down to 0 when the band edge for the Dirac cone is reached at the bottom surface, similar to the case of the single barrier.

The k_x-resolved and total DOSs projected on the surface atoms are plotted in Fig. 9, where the bound state can be clearly seen in the 4-QL region extending from 10 to 60 Å. The DOS associated with this bound state oscillates and decays towards the center of the quantum well defined by the two barriers at the step edges. A band bending similar to that observed for the single barrier is also seen for this particular

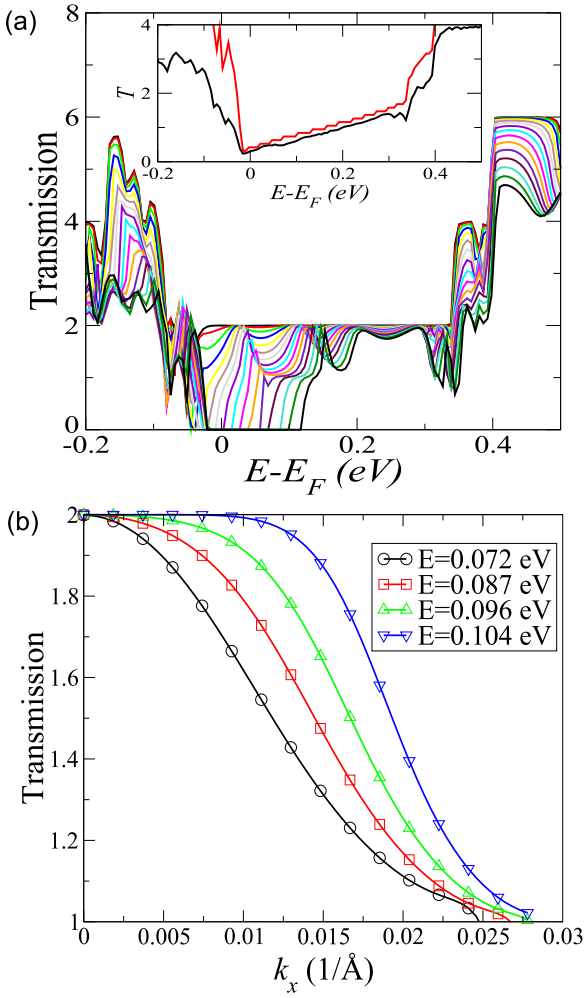

FIG. 8. (Color online) (a) The transmission across the double surface barrier at different k_x. Similarly to the single-barrier case, $T = 2$ for $k_x = 0$ but then reduces at other angles of incidence. Note also the Fabry-Perot type oscillations in transmission, which are not present in Fig. 2(a). Different curves correspond to different k_x values, from $k_x = 0$ up to $k_x = 0.034\,75$ Å^{-1}, in equal steps of $0.002\,317$ Å^{-1}. Inset: The integrated transmission obtained with (black curve) and without [gray (red) curve] the barriers. (b) The transmission as a function of k_x at different constant energy cuts. These energies are chosen away from the resonances.

barrier configuration. The interaction between the bound states localized at the two barriers splits them in energy, creating alternating high and low DOSs as one moves up along the energy axis. Another noticeable feature is a state localized in the 4-QL region at around 0.1 eV [see Fig. 9(b)]. This is an additional state in the 4-QL slab, which is decoupled from the 3-QL leads. The same state is absent in the case of a single barrier produced by a step edge between a 3-QL and a 4-QL semi-infinite lead. The Fourier transforms of the DOS display features similar to those shown in Fig. 3. However, in the double-barrier case the resolution is improved over that of the single-barrier structure since we now have more atoms along the flat region next to the barrier.

We also study the energy dispersion of the quasibound state obtained at the barrier, by calculating the PDOS on the Se atom

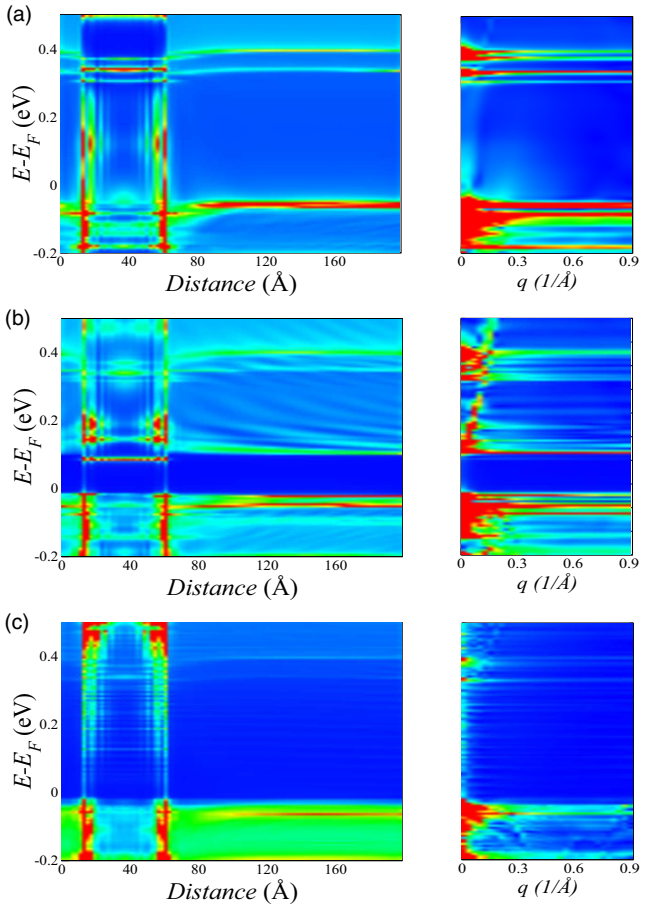

FIG. 9. (Color online) DOS projected on the surface atoms along the double-barrier scattering region at (a) $k_x = 0$, (b) at $k_x = 0.032$ Å^{-1}, and (c) integrated over all k_x. Note the absence of density oscillations for $k_x = 0$ and for the integrated DOS. The incidence at finite k_x leads to density oscillations clearly seen in the long flat region adjacent to the barrier as shown in (b). The panels at the right are the corresponding Fourier transforms, which are featureless in (a) and (c), while clearly showing the presence of scattering in (b).

at the barrier, as a function of $E - E_F$ and momentum along step (k_x). This is shown in Fig. 4(d), with a comparison to the band structure of the unperturbed periodic system. Apart from the Dirac bands, additional states, dispersing along k_x, are visible at the interface. These have a dispersion very similar to that in the case of a single barrier [see Fig. 4(b)]. However, some additional features are seen when this pair of states mixes with the Dirac bands, with an alternating pattern of higher and lower PDOSs being visible. This is due to the interaction between the bound states at the two barrier edges. Away from the interface the PDOS and the dispersion revert to those of the pristine system with only the Dirac bands being present.

Note that for this particular chosen length of the double barrier there are no quantum well states formed inside the 4-QL region. However, for a longer barrier the quantum well states appear, as demonstrated by the PDOS on the surface atoms at two k_x values for a barrier of length 149.16 Å (see Fig. 10). At normal incidence no quantum well states can be formed in the energy window of the surface state, since the

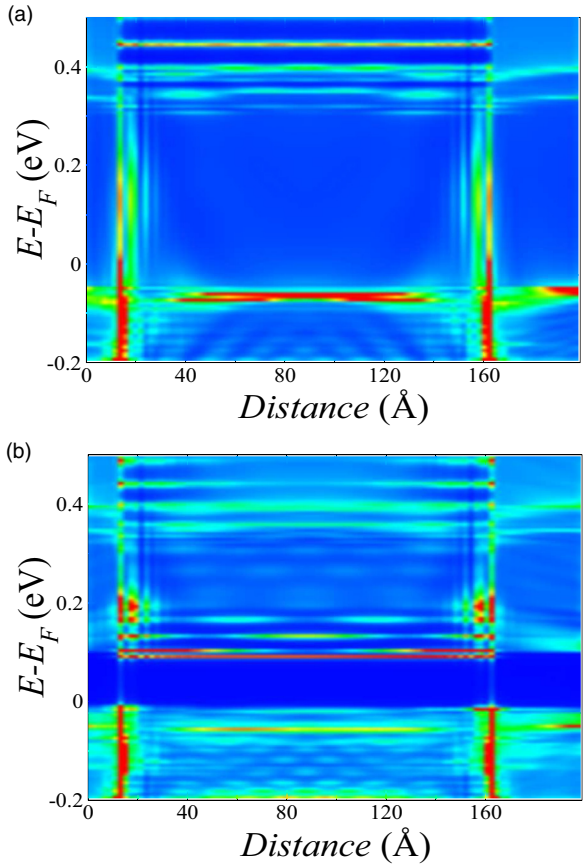

FIG. 10. (Color online) PDOS on the surface atoms for a double barrier of length 149.16 Å at (a) $k_x = 0$ and (b) $k_x = 0.032$ Å^{-1}. Note the absence of quantum well states in (a). In (b) quantum well states interact with the bound state at the two barriers, leading to energy splitting of the bound state.

two surface states have opposite spin projections, leading to no interference. In contrast, at finite k_x quantum well states appear (e.g., a nodeless state at around 0.13 eV and a single-node state at around 0.16 eV). However, the behavior of these states near the edges of the barrier is different from usual because of the presence of the bound state. In fact, these quantum well states interact with the bound states at the edges of the barrier, resulting in an energy splitting of the bound state. We observe splitting of the bound states in both the short and the long double barrier, in the former case due to the interaction between the bound states located at the two edges of the 4-QL region, while in the latter due to the bound state interacting with the quantum well state within the barrier.

VI. SUMMARY

We have used *ab initio* transport theory to study scattering to both single and double barriers of the topological protected states present on a Bi_2Se_3(111) surface. In particular, we have studied the dependence of the transmission on the angle of incidence and the electron energy. At normal incidence our first-principles approach confirms Klein tunneling. Furthermore, we have calculated the DOS projected on the surface atoms and found bound states localized only on the higher

side of the barrier. Thus our LDOS plots make apparent the three-dimensional nature of the scattering problem, in which the spins of the surface states are no longer confined to the plane of the topological insulator slab. We have also constructed a simplified potential barrier model using linear Dirac bands to compare with our first-principles calculations. Throughout this paper we have placed our results in the context of recent experimental work.

ACKNOWLEDGMENTS

A.N. thanks the Irish Research Council for financial support. I.R., A.D., and S.S. acknowledge additional financial support from KAUST (ACRAB project). Computational resources were provided by the Trinity Centre for High Performance Computing and the Irish Centre for High-End Computing (ICHEC).

[1] H. Zhang, C.-X. Liu, X.-L. Qi, X. Dai, Z. Fang, and S.-C. Zhang, Nat. Phys. **5**, 438 (2009).
[2] Y. Xia, D. Qian, D. Hsieh, L. Wray, A. Pal, H. Lin, A. Bansil, D. Grauer, Y. S. Hor, R. J. Cava, and M. Z. Hasan, Nat. Phys. **5**, 398 (2009).
[3] D. Pesin and A. H. MacDonald, Nat. Mater. **11**, 409 (2012).
[4] M. Z. Hasan and C. L. Kane, Rev. Mod. Phys. **82**, 3045 (2010).
[5] H. Beidenkopf, P. Roushan, J. Seo, L. Gorman, I. Drozdov, Y. S. Hor, R. J. Cava, and A. Yazdani, Nat. Phys. **7**, 939 (2011).
[6] J. Wang, W. Li, P. Cheng, C. Song, T. Zhang, P. Deng, X. Chen, X. Ma, K. He, J.-F. Jia, Q.-K. Xue, and B.-F. Zhu, Phys. Rev. B **84**, 235447 (2011).
[7] Z. Alpichshev, R. R. Biswas, A. V. Balatsky, J. G. Analytis, J.-H. Chu, I. R. Fisher, and A. Kapitulnik, Phys. Rev. Lett. **108**, 206402 (2012).
[8] S. Kim, M. Ye, K. Kuroda, Y. Yamada, E. E. Krasovskii, E. V. Chulkov, K. Miyamoto, M. Nakatake, T. Okuda, Y. Ueda, K. Shimada, H. Namatame, M. Taniguchi, and A. Kimura, Phys. Rev. Lett. **107**, 056803 (2011).
[9] T. Zhang, P. Cheng, X. Chen, J.-F. Jia, X. Ma, K. He, L. Wang, H. Zhang, X. Dai, Z. Fang, X. Xie, and Q.-K. Xue, Phys. Rev. Lett. **103**, 266803 (2009).
[10] Z. Alpichshev, J. G. Analytis, J.-H. Chu, I. R. Fisher, Y. L. Chen, Z. X. Shen, A. Fang, and A. Kapitulnik, Phys. Rev. Lett. **104**, 016401 (2010).
[11] Z. Alpichshev, J. G. Analytis, J.-H. Chu, I. R. Fisher, and A. Kapitulnik, Phys. Rev. B **84**, 041104(R) (2011).
[12] X. Zhou, C. Fang, W.-F. Tsai, and J. P. Hu, Phys. Rev. B **80**, 245317 (2009).
[13] R. R. Biswas and A. V. Balatsky, Phys. Rev. B **83**, 075439 (2011).
[14] R. R. Biswas and A. V. Balatsky, Phys. Rev. B **81**, 233405 (2010).
[15] X.-F. Wang, Y. Hu, and H. Guo, Phys. Rev. B **85**, 241402(R) (2012).
[16] T. Nakanishi, M. Koshino, and T. Ando, Phys. Rev. B **82**, 125428 (2010).
[17] J. M. Soler, E. Artacho, J. D. Gale, A. Garcia, J. Junquera, P. Ordejón, and D. Sánchez-Portal, J. Phys.: Condens. Matter **14**, 2745 (2002).
[18] A. R. Rocha, V. M. Garcia-Suarez, S. Bailey, C. Lambert, J. Ferrer, and S. Sanvito, Nat. Mater. **4**, 335 (2005).
[19] A. R. Rocha, V. M. Garcia-Suarez, S. Bailey, C. Lambert, J. Ferrer, and S. Sanvito, Phys. Rev. B **73**, 085414 (2006).
[20] I. Rungger and S. Sanvito, Phys. Rev. B **78**, 035407 (2008).
[21] L. Fernández-Seivane, M. A. Oliveira, S. Sanvito, and J. Ferrer, J. Phys.: Condens. Matter **18**, 7999 (2006).
[22] J. P. Perdew, K. Burke, and M. Ernzerhof, Phys. Rev. Lett. **77**, 3865 (1996).
[23] B. Naydenov, M. Mantega, I. Rungger, S. Sanvito, and J. J. Boland, Phys. Rev. B **84**, 195321 (2011).
[24] M. I. Katsnelson, K. S. Novoselov, and A. K. Geim, Nat. Phys. **2**, 620 (2006).
[25] I. A. Nechaev, M. F. Jensen, E. D. L. Rienks, V. M. Silkin, P. M. Echenique, and E. V. Chulkov, and Ph. Hofmann. Phys. Rev. B **80**, 113402 (2009).
[26] M. F. Crommie, C. P. Lutz, and D. M. Eigler, Nature **363**, 524 (1993).
[27] I. Rungger, A. Narayan, U. Schwingenschloegl, and S. Sanvito (unpublished).
[28] M. L. Teague, H. Chu, F.-X. Xiu, L. He, K.-L. Wang, and N.-C. Yeh, Solid State Commun. **152**, 747 (2012).
[29] J. Seo, P. Roushan, H. Beidenkopf, Y. S. Hor, R. J. Cava, and A. Yazdani, Nature **466**, 343 (2010).
[30] A. Narayan, I. Rungger, and S. Sanvito, Phys. Rev. B **86**, 201402(R) (2012).
[31] The plots were generated using XCrySDen software: A. Kokalj, Comp. Mater. Sci. **28**, 155 (2003).
[32] Y. Takane and K.-I. Imura, J. Phys. Soc. Jpn. **81**, 093705 (2013).
[33] Y. Takane and K.-I. Imura, J. Phys. Soc. Jpn. **82**, 074712 (2013).